Chapter 3: Subduction Transition and Flat Slab

Structure of the Subduction Transition Region from Seismic

Array Data in Southern Peru

Kristin Phillips and Robert W. Clayton

Abstract

Data from three seismic arrays installed in southern Peru was analyzed using receiver functions from P, PP, and PKP wave phases, in order to image the subducted Nazca slab. The arrays cover the transition region from flat slab subduction in central Peru to normal subduction with an angle of about 30˚ further south. The results provide an image of the flattened slab from the coast to approximately 300 km inland and also across the transition region from flat to 30-degree subduction, which appears to be a bend rather than a tear in the slab. In the flat slab region, the slab is well defined near the coast and flattens out at 100 km depth beneath the Altiplano. The slab appears to start flattening some 400 km in advance of the subduction of the Nazca Ridge and the flattening is maintained for 1300 km after its passage. The Moho begins at a depth of around 30 km near the coast and has a maximum depth of 75 km beneath the Altiplano, consistent with the results of the other arrays. The Vp/Vs ratios for both arrays exhibit average values between 1.73 and 1.75 indicating that the region is most likely not actively volcanic. The images also show a positive-impedance midcrustal structure at

around 40 km depth, which is suggested to be a result of underthrusting of the Brazilian

shield. This would explain the missing crust needed to support the Altiplano.

3.1. Introduction

The dip of the subducted Nazca plate beneath southern Peru changes from shallow or

flat slab beneath central Peru to a steeper dip angle ("normal" subduction) of around 30

degrees beneath southern Peru. This transition is evident in the seismicity (Barazangi &

Isacks, 1976; Cahill and Isacks, 1992; Grange et al, 1984; Suarez et al, 1983), and by a

gap in the arc-volcanism (Gutsher, Olivet et al, 1999; Gutscher, Spakman et al. 2000;

McGeary et al, 1985). Adakitic magmas have also been associated with flat slab

regions (Gutscher, Maury, et al. 2000) and have been reported in southern

Ecuador/northern Peru (Beate et al, 2001). They are suggested to result from partial

melting of subducted oceanic crust (Gutscher, Maury, et al. 2000). Besides the

observed correspondence between adakites and flat slab regions, the partial melting

resulting in such magmas could also be a result of slab tearing at the transitions from

flat slab to a steeper dip angle (Yogodzinski et al, 2001). The lack of reported adakites

in southern Peru might indicate that the southern transition is slab bending rather than a

tear. The change in dip is coincident with the subduction of Nazca Ridge. This is one

of three zones of slab-dip changes along the western margin of Southern America. In

central Chile, the subduction of the Juan Fernandez Ridge is cited as the cause of the

flattening along its subduction trajectory (Pilger, 1981; Gutscher, Spakman et al, 2000;

von Huene et al, 1997), and the study of Anderson et al (2007) show that the zone of

flattening tightly conforms to the shape of the ridge. In Equador, the Carnegie Ridge also apparently causes the slab to flatten (Gutscher,Malavielle et al. 1999).

Various mechanisms have been proposed as to the cause of flat slab subduction. Some authors have noted a correlation between regions of flat slab subduction and the presence of thickened oceanic crust such as that due to a subducting plateau or ridge which could increase the buoyancy of the subducting slab (Gutscher, Maury et al. 2000). Gutscher et al. (1999) proposed that the length of flat subduction in Peru was due to buoyancy effects resulting from two subducting ridges; the Nazca ridge and a previously unknown impactor referred to as the Inca Plateau which is believed to be the mirror image of the Marquesas plateau although recent plate movement reconstructions call into question the proposed location and timing of the Inca plateau (Skinner and Clayton 2012). Both plateaus were suggested to have formed at the Pacific-Farallon spreading centre based on tectonic reconstructions. According to Hampel (2002), the Nazca Ridge originally began subducting at 11°S around 11.2 Ma. Since then it has been sweeping south and presently has a migration rate of around 43 cm per year. The area of flat subduction in Peru corresponds to the area swept out by the Nazca Ridge. Thus the Nazca Ridge may have had an impact on the evolution and shape of the subduction zone. In addition to buoyancy effects caused by a subducting ridge or plateau, other factors could influence flat subduction such as the age of the lithosphere being subducted (Sacks 1983), delay in the basalt to eclogite transformation (Gutscher, Spakman et al. 2000; Pennington 1984), absolute motion of the upper plate (Olbertz et al. 1997), the convex curvature of the Peruvian margin (Bevis, 1986; Cahill and Isacks,

1992), intraplate hydrostatic suction (Jischke, 1975), or cycles of flat subduction

caused by rebound after a steepening slab breaks off (Haschke et al, 2002). Modeling

has been done in several studies to address the relative importance of different causes

for flat slab subduction. Van Hunen et al (2002a) suggested that relative motion of the

upper plate could be equally or more important than plateau subduction based on

numerical studies; however this is a factor that is present in the region of normal

subduction as well. The dominant mechanism for flat slab subduction needs to be

considered independently for each subduction zone since some factors are present in

both normal and flat slab regions, while other factors can be observed in only some flat

slab regions and not in others. One of the puzzling aspects of the flat subduction in

southern Peru is the fact that the slab does not return to a normal dip angle after the

impactor has passed. This contrasts with central Chile where the slab returns to normal

dip at a distance of about 150 km on either side of the track of the JFR (based on

contours from Anderson et al, 2007).

In this study, we examine the details of the transition zone between normal and flat

subduction using dense seismic arrays, which include instruments both in the flat-slab

zone as well as an array parallel to the trench to sample the subduction transition. The

array in the flat slab region near the Nazca Ridge provides an opportunity to study the

effect of the Nazca Ridge on the subduction zone in Southern Peru. A previous study

(Phillips et al, 2012) has described the results of a line (Line 1, figure 3.1) that is in the

normal-dip part of the zone. It succeeded in imaging the slab down to 250 km, and

found a midcrustal velocity increase at about 40 km depth suggested to be

underthrusting by the Brazilian shield. In this study we expand on those results by
presenting details of the transition and flat slab subduction regions.

Receiver function studies performed here provide details of the structure of the
subduction system including Moho depth and shape of the slab as well as velocity
information such as Vp/Vs ratio. Corresponding images show the transition from
normal to flat slab subduction and the shape of the slab in the flat slab region, which is
affected by the subducting Nazca Ridge. The structure of the flat slab region is
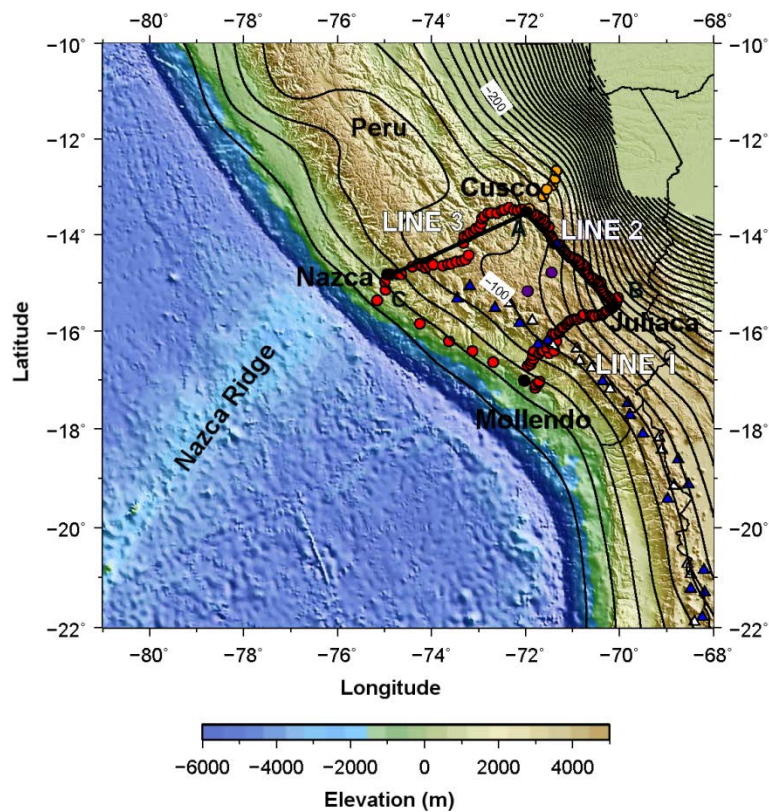compared to the study of the normal subduction regime.

Figure 3.1. Location of the seismic arrays in Southern Peru as denoted by red circles.
Added stations from the PULSE and CAUGHT experiments are shown as orange and
purple circles respectively. The topography and bathymetry shows the incoming Nazca

Ridge and the Altiplano of the Andes. Slab contours are based on fits to seismicity and comes from the Slab 1.0 model (Hayes et al, 2012). Active and dormant volcanoes are denoted by white and blue triangles.   The three seismic arrays are labeled "Line 1," "Line 2," and "Line 3." Line 1 is located in the region of normal subduction, Line 2 samples the transition from normal to flat slab subduction, and Line 3 is in the flat slab region. The black lines along Lines 2 and 3 with endpoints labeled A, B, and C correspond to cross section profiles in figure 3.2.

3.2. Methods

3.2.1 Stations and Data

Three lines of broadband sensors were installed as part of the Peru Subduction Experiment (PeruSE) as seen in figure 3.1. The first line (Line 1) deployed perpendicular to the trench from Mollendo on the coast to Juliaca near Lake Titicaca, samples the region of normal subduction dip (Phillips et al, 2012). The second seismic array (Line 2) runs parallel to the trench from Juliaca to Cusco sampling the transitional region where the subduction regime changes to shallow subduction. It includes 50 broadband seismic stations over a distance of about 300 km resulting in an average station spacing of about 6 kilometers. Line 3 is perpendicular to the trench starting on the coast near the city of Nazca and runs inland through Cusco for 509 km. It consists of 40 stations from the PeruSE network plus 5 stations from the PULSE network (Eakin et al, 2011). Line 3 is located near where the Nazca Ridge is subducting beneath South America and samples the flat slab region. In addition, 2 stations from the CAUGHT network (Ryan et al, 2011) that are in the interior of the box defined by the networks described above are used.
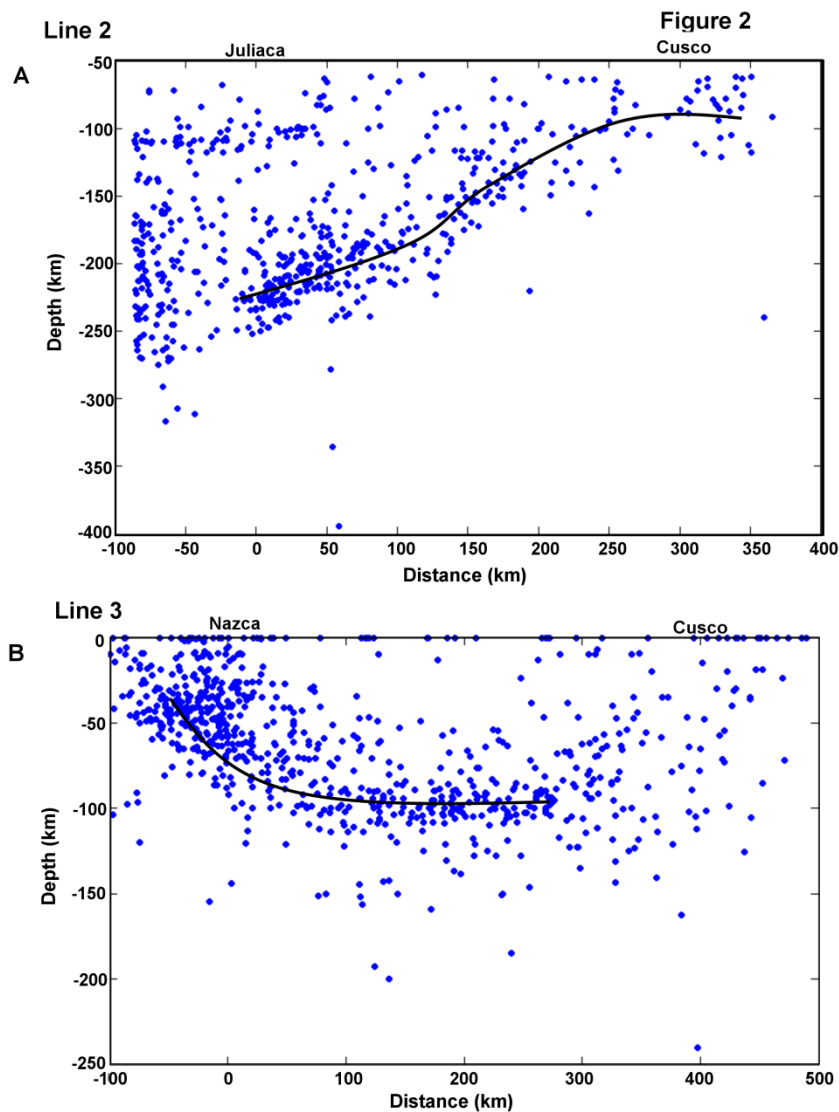
Figure 3.2. Seismicity cross-sections along the projections of Lines 2 and 3 shown as black lines in figure 3.1. Earthquakes locations are from the ISC reviewed catalogue (International Seismological Centre, 2010). The black lines show the estimated slab location from seismicity. (A) Seismicity crosssection parallel to the trench from Cusco to Juliaca as shown as black line A-B in figure 3.1. Cusco is located in the region of flat slab subduction while Juliaca further south is in the region of normal subduction . (B) Seismicity crosssection from Nazca to Cusco in the region of flat slab subduction shown by line C-B in figure 3.1.

The flat slab and the transition from normal to flat slab subduction can be roughly

delineated by the seismicity of the Wadati-Benioff zone as is shown in figure 3.2. Event

locations are from the ISC reviewed catalog. The black lines show an average value for slab location based on best fit to seismicity. The seismicity shows the slab flattening out at 100 km depth beneath the Altiplano in the flat slab region and the shape of the curve in the transition region between Cusco and Juliaca.

Teleseismic data collected by the array was used in receiver function studies. Earthquakes between 30 and 90 degrees away from Peru were used to make receiver functions based on the P wave arrival. However since many events are located beyond 90 degrees from Peru, PP and PKP phases were also analyzed for events occurring at distances greater than 90 degrees distance from Peru. PKP phases are used at distances between 143 and 180 degrees and can be useful for detecting dipping interfaces. For Line 2, a total of 73 events using the P wave phase, 175 PP and 50 PKP wave phase events were used in this study. For Line 3, 50 P wave, 106 PP and 21 PKP phase events were used. To ensure higher signal to noise, events are of magnitude 5.8 or greater for distances less than 90 degrees from Peru and greater than magnitude 6.0 for distance greater than 90 degrees. The data was generally bandpassed from 1 to 100 seconds, but this was narrowed to 2–100 seconds for some distant events with higher apparent noise. Data was included if the signal to noise ratio appeared adequate for both the raw seismic data and resultant receiver functions.

3.2.2 Receiver Functions

Receiver functions were formed using the method described in Langston (1979) and Yan and Clayton (2007). Mantle and source effects are minimised by deconvolving the radial with the vertical component in the frequency domain (Langston, 1979; Ammon,

1991). Time domain iterative deconvolution (Ligorria and Ammon, 1999) was also

tried, but produced noiser results. Receiver functions were stacked using the method of

Zhu and Kanamori (2000) using multiple events from a similar backazimuth for each

station to perform stacks. A maximum weighted summation function for stacking over

the Moho and multiple arrivals provides estimates for depth to the impedance contrast

and the Vp/Vs ratio. Average crustal P wave velocities used in the estimate of depth

and Vp/Vs from stacking of receiver functions for each station were derived mostly

from averages of the 3D P wave velocity structure of Cunningham and Roecker (1986)

for southern Peru. Their model was also compared with more recent velocity models

such as the model of Dorbath et al (2008) from northern Chile. Uncertainty in the

stacking method described above is given by the 95% maximum contour. Estimates of

depth uncertainty due to uncertainty in the velocity model used for stacking are on the

order of 2 km or less based on performing stacks with variations in average crustal Vp

of up to 0.2 km/sec from the velocity model used.

Receiver function images were produced by backprojecting along rays from the

direction that the energy arrived to plot receiver function amplitudes as a function of

distance and depth. A simple velocity model based on IASP91 was used for the

conversion from receiver function time to depth.

In addition to backprojected images, receiver function migration is done using

information about the station, ray parameter, incidence angle, and a simple

homogenous half space velocity model. A starting model uses an average crustal P

wave velocity of 6.3 and the average Vp/Vs ratio of 1.75. The velocity was varied to test sensitivity of the migration results to the velocity.

3.2.3 Finite Difference Modeling

 A simple 2D velocity model was used to produce synthetic receiver functions using a 2D finite difference code (Kim et al, 2010) to compare with receiver function results for both Lines 2 and 3. The model for Line 2 is 300 km wide in distance and 250 km in depth. It has an average crustal P-wave velocity of 6.3 km/sec with a midcrustal velocity jump to 6.6 km/sec. The velocity jump is constrained by the amplitude of the midcrustal arrival. The mantle wedge is taken as having an average velocity of 7.7km/sec and the subducting oceanic crust as 7.0 km/sec (Abers et al, 2006; Abers, 2000; Kim et al 2010). The underlying mantle is taken as having an average velocity of 8.0 km/sec down to 250 km. Synthetic receiver functions are produced by modeling plane waves with variable ray parameters to simulate teleseismic sources.
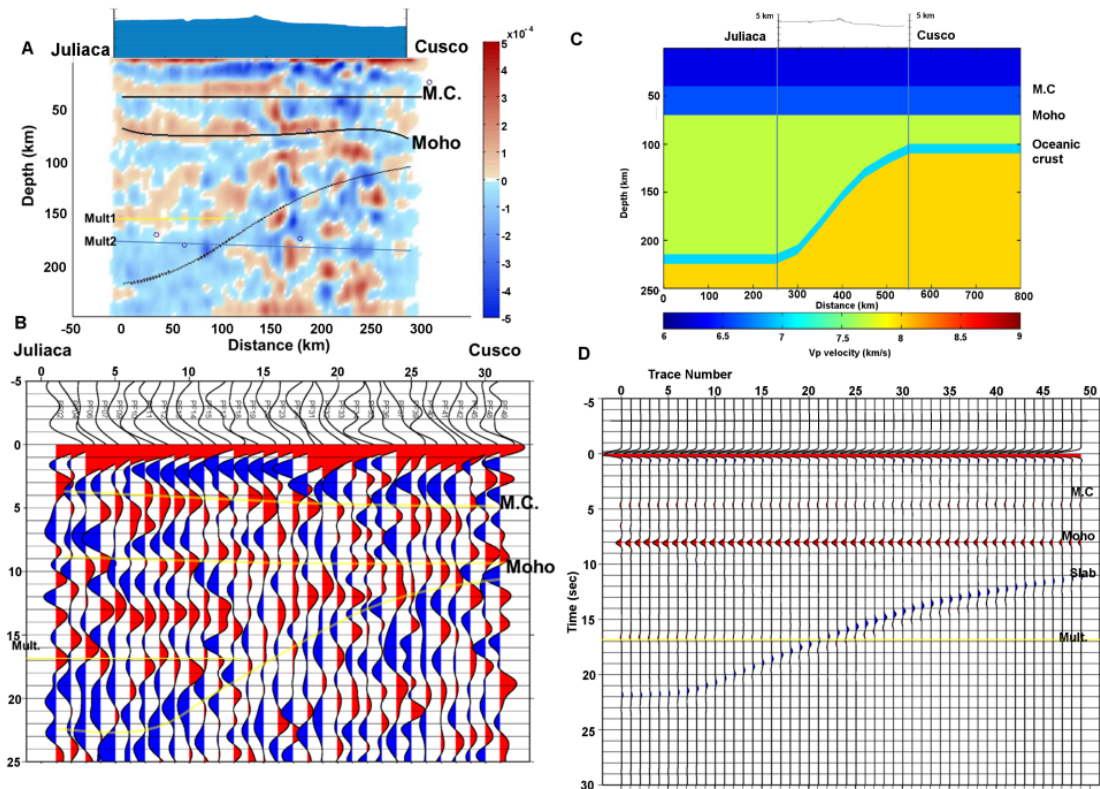
Figure 3.3. Results from Line 2 showing the transition from normal subduction in the southernmost part of Peru near Juliaca to shallow or flat slab subduction to the north near Cusco. (A) Receiver function image for Line 2 based on stacks of P and PP receiver functions for each station. Distance from Juliaca in kilometers is plotted against depth in kilometers. The black lines show a positive impedance midcrustal structure at around 40 km depth, the Moho at around 70–75 km depth, and the shape of the slab which is deliniated primarily by a negative impedance signal. Also observable is a positive impedance arrival above the negative slab signal which also appears to be related to the slab. The positive pulse can be compared to the positive slab arrival for Line 1 in figure 3.12B. (B) The receiver function plot below shows receiver functions from a magnitude 7.3 earthquake occurring near Vanuatu Islands on August 10, 2010. (C) Simple 2D P-wave velocity model used for finite difference modeling based on receiver function results. (D) Synthetic receiver functions from finite difference model showing P wave arrival, midcrustal structure, Moho, slab, and multiple arrival.

3.3. Results

3.3.1 Line 2 Results: Transition From Normal to Flat Slab Subduction

Line 2 samples the transition from normal to flat subduction. On the SE end (near Lake

Titicaca) the slab is at a depth of approximately 215 km, while on the NW end (near

Cusco) the slab is at a depth of 100km An image of the Moho and the slab can be seen

in the receiver functions shown in figure 3.3A. Also observable is a midcrustal positive

impedance signal at a depth of about 40 km, which was interpreted by Phillips et al

(2012) to result from the underthrust Brazilian Shield. The strength of the midcrustal

signal relative to the Moho can be seen in the supplementary materials which show that

a very similar Moho and midcrustal signal are seen at multiple stations across the array.

Both features appear to be relatively flat and the Moho has an average depth between

70 and 75 km beneath the Altiplano. This depth is consistent with the relatively flat

elevation profile and suggests that the topography is isostatically supported by the

crustal root (see figure 3.9 which shows consistency with Airy Isostasy). Receiver

function traces from a magnitude 7.3 Vanuatu earthquake on August 10, 2010 (figure

3.3B) shows a result consistent with all other receiver function images based on

multiple events. The receiver function traces show signals from the midcrustal

structure, Moho, slab, and crustal multiples. Finite-difference modeling based on

receiver function results for Line 2 using a simplified 2D velocity model produces

synthetic receiver functions consistent with the receiver function data (figure 3.3C,D).

Common conversion point (CCP) stacks were done for both the P/PP and PKP receiver

functions and the resultant images are shown in figure 3.4 which is consistent with

figure 3.3A. Although the primary slab signal observed for Line 2 is a negative

impedance signal consistent with finite difference modeling results, a positive

impedance signal roughly following the shape of the slab is observed above the

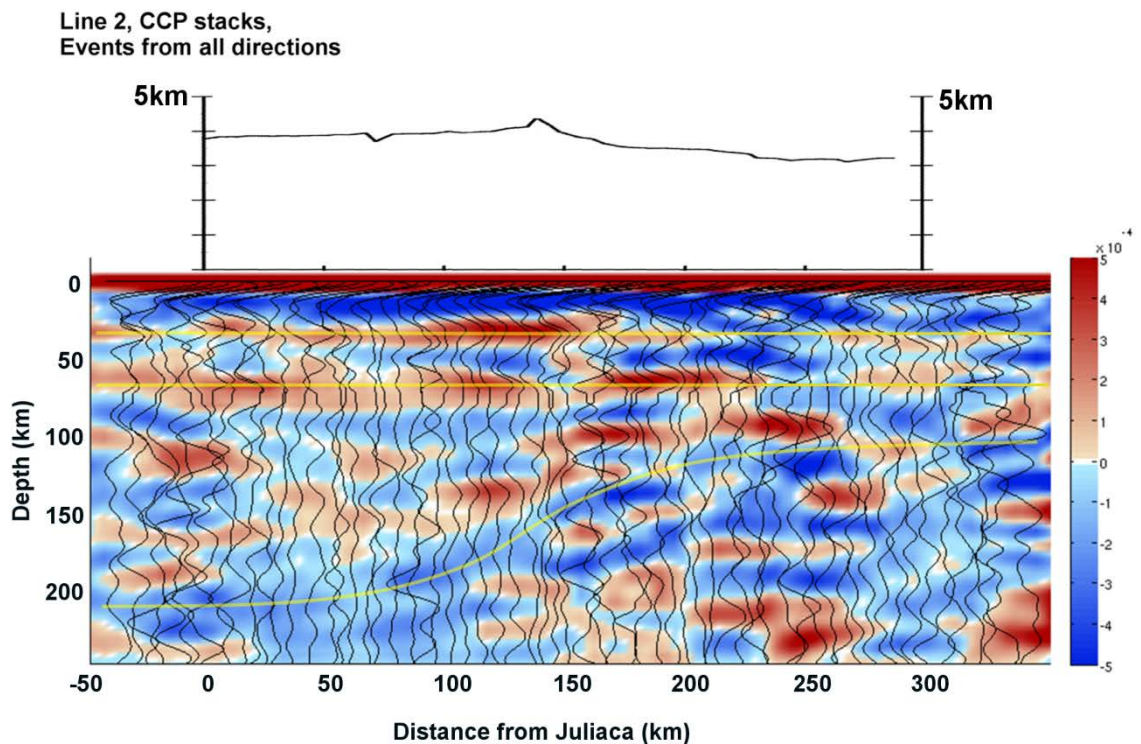negative slab signal as seen in figures 3.3 and 3.4.

Figure 3.4. Plot of common conversion point (CCP) stacks with bin spacing equal to
station spacing. The stack traces are shown overlying the amplitude of the stack with
some horizontal smoothing. Receiver functions included in the stacks come from all
azimuthal directions. The images show the midcrustal structure, Moho signal (positive
impedance signals) which are both relatively flat, and the slab signal which is observed
as a negative impedance signal underlying a positive slab arrival. The station elevation
is shown above the image (note the different scale from the CCP image).

Another check on the shape of the slab is receiver function migration using a simple

homogenous velocity model for the crust. The results are shown in figure 3.5 which

shows a discontinuous signal from the Moho and midcrustal structure and a clear

change from negative to positive impedance near where the top of the slab is expected.
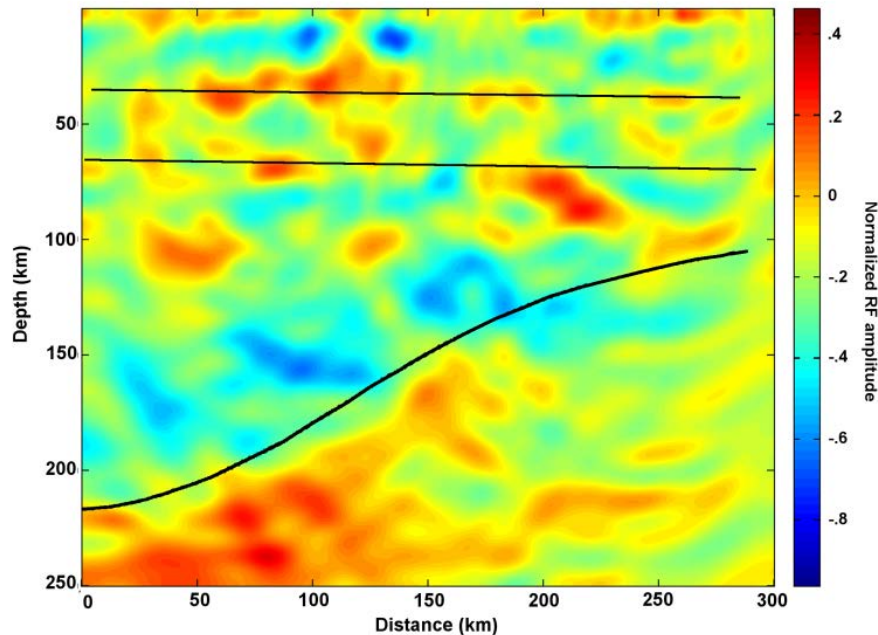

Figure 3.5. Line 2 receiver function migration plotted as distance from Juliaca on the x-axis and depth on the y-axis. Black lines show an interpretation of the image showing the expected location of the midcrustal structure, Moho, and slab. Notice the change from negative to positive receiver function impedance corresponding with the expected location of the slab.

Several different models for the shape of the slab were considered and modeled using

the finite difference method for comparison with the receiver function data, including a

linear transition, an abrupt transition consistent with a slab break, and a gently curving

model shown in figure 3.3 (see supplementary materials for alternative models). The

receiver function results such as figure 3.4 best match the gradually curving model.

The Moho and Vp/Vs results obtained from receiver function stacking using the

method of Zhu and Kanamori (2000) are summarized in figure 3.9, which shows station

elevation, Moho depths, and Vp/Vs ratios. The Moho is relatively flat for Line 2 and

increases with depth to a maximum depth of 75 km near Line 3 with a decrease in

crustal thickness noticeable where station elevation begins to decrease.
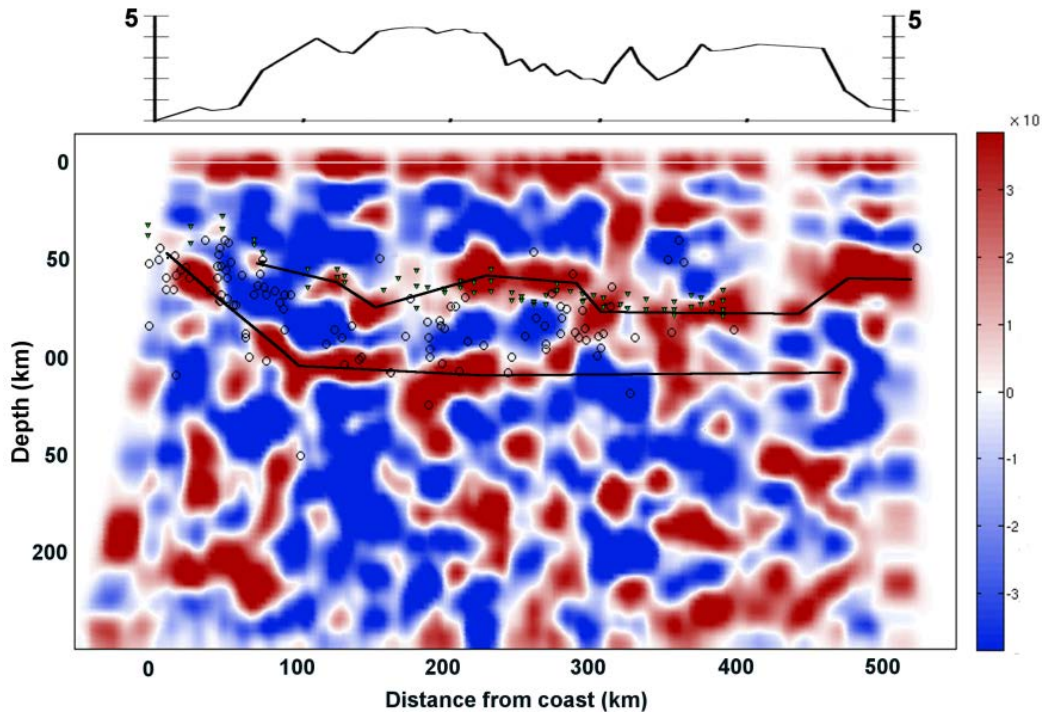
Line 3 RF Results, P/PP phase, NW baz

Figure 3.6. Receiver function image for Line 3 based on P and PP receiver functions
from a NW azimuth from Peru. The image was formed by backprojecting the rays
from the direction in which the energy originated. Distance is from the coast near
Nazca to Cusco. Black lines show an interpretation of the Moho with individual station
picks from stacking shown as green triangles, and interpretations of the slab and
midcrustal structure. The slab can be seen flattening out at 100 km depth with the
Moho just above it at around 70 km depth. Note a shallowing of Moho depth between
about 200 and 300 km distance and near 500 km distance where topography decreases
in elevation, indicating a good correspondence between topography and Moho depth.

3.3.2 Line 3 Results: Flat Slab Region

The third seismic array runs from the coast near Nazca northeast to Cusco in the region

of shallow subduction just south of where the continuation of the Nazca Ridge is

subducting.   The shallow slab can be clearly seen to a depth of about 100 km in figure

3.6, as well as the Moho at an average depth of 70 to 75 km. A midcrustal structure is

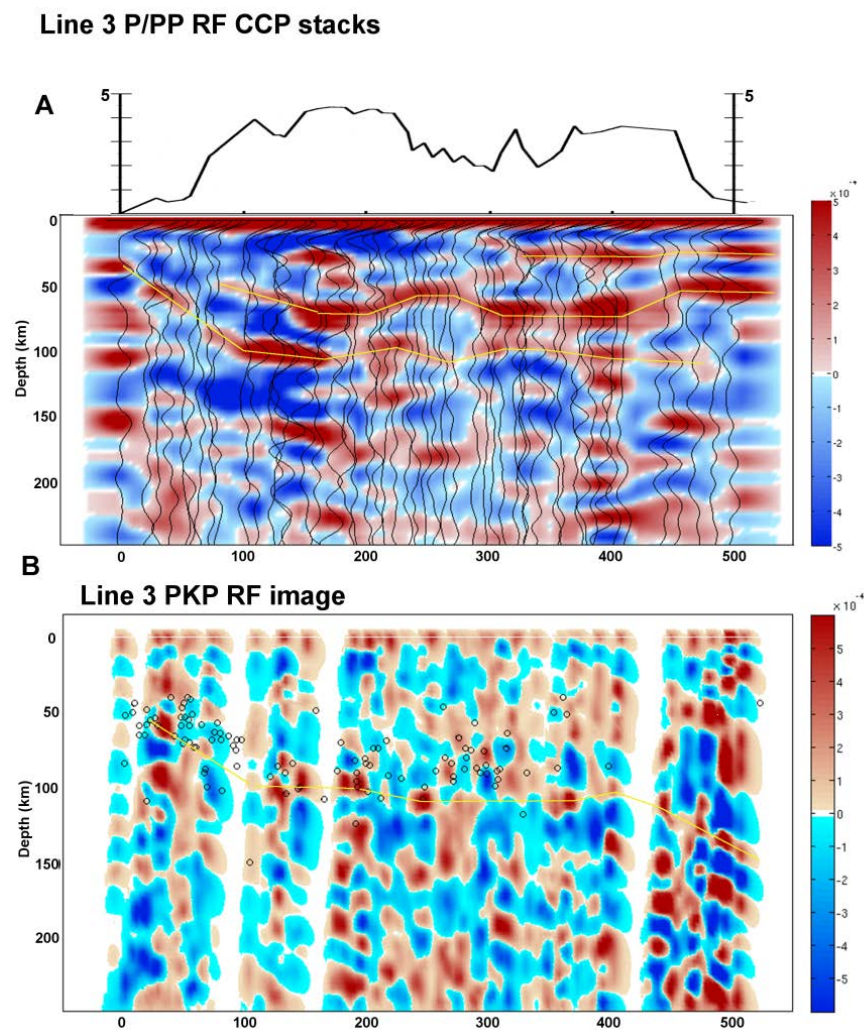observed as well (see figure 3.7A for clarification).

Figure 3.7. (A) CCP plot for Line 3 showing the stacks with background colours showing amplitude. The midcrustal structure, Moho, and slab interpretations are delineated with yellow lines (B) PKP image for Line 3 for comparison. Note that the Moho is less well defined but the slab is visible and appears to descend in the eastern-most stations.

 The receiver function traces from the NW backazimuth in figure 3.8B also show the

Moho signal clearly as well as the signal from the slab as it flattens at 100 km depth. A

more complete image showing that the slab remains flat for the extent of the array can

be seen in the CCP stacks plotted in figure 3.7A. The same slab signal is also seen in

an image based on PKP receiver functions which appears to show that the Nazca plate

begins descending deeper into the mantle at a distance of about 450 km from the start

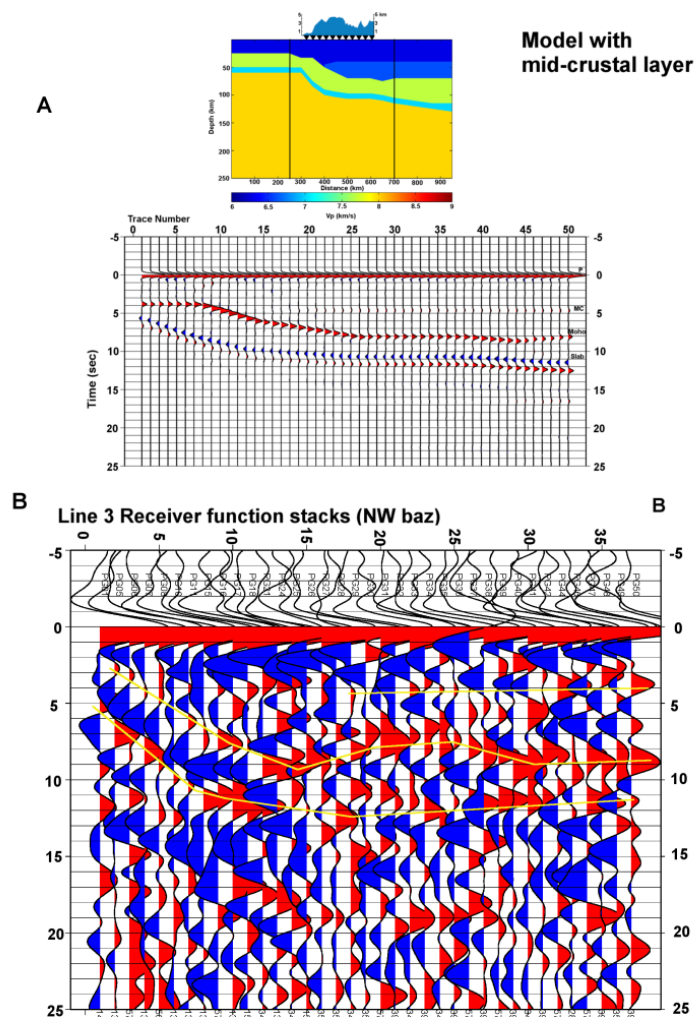of the seismic array (figure 3.7B).

Figure 3.8. (A) Finite difference modeling for Line 3. The model includes a midcrustal velocity increase. Synthetic receiver functions are consistent with receiver function

results showing the double pulse structure of the slab, the positive Moho signal, and midcrustal structure.

(B) Receiver function plot showing stacks for each station based on events from the northwest consistent with the images in figure 3.6. Major arrivals such as the slab signal, Moho depth, and midcrustal structure are marked by yellow lines and can be compared to the synthetics in part A.

The receiver function results can be compared to 2D finite-difference models as in figure 3.8A. The model that fits the data best includes a velocity increase between the upper and lower crust. The synthetic receiver functions show a double pulse structure the full length of the subducting oceanic crust which is consistent with figure 3.7A which includes receiver function data from all azimuths while in single azimuth images such as figure 3.6 the positive impedance signal from the base of the oceanic crust is more difficult to detect at greater distances and depths.
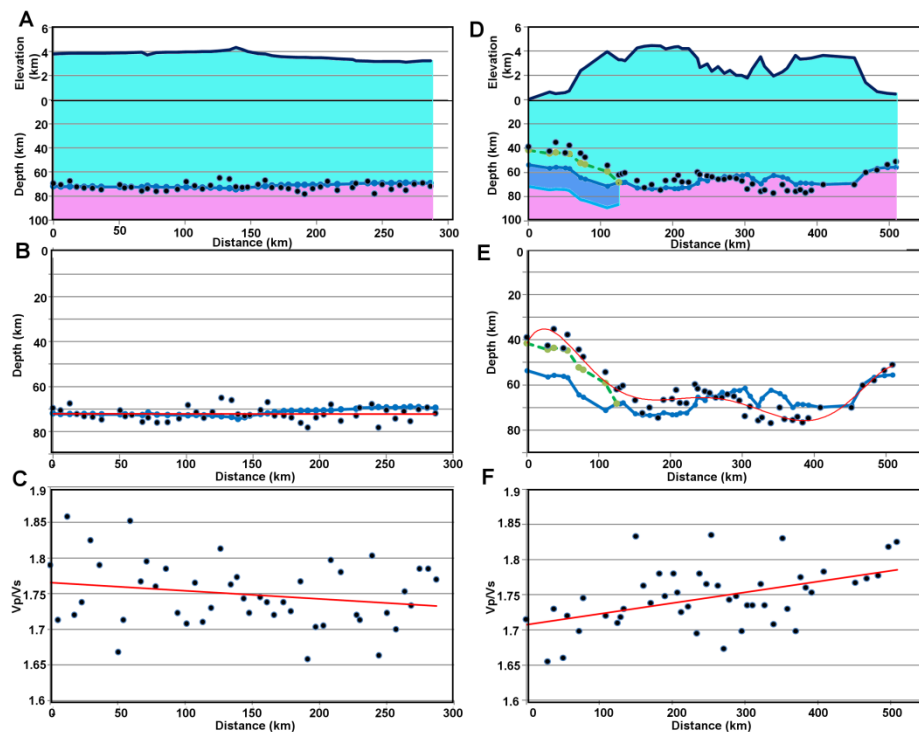

Figure 3.9. Moho and Vp/Vs results for Lines 2 and 3.   A) Isostasy model for Line 2 including station elevation. Note the differing scales between elevation and Moho

depth. The blue line is a calculation of expected depth for Airy isostasy relative to a reference station assuming an average crustal density of 2.7g/cc and average mantle density of 3.3g/cc. B) Line 2 Moho depth from stacking. The red line shows a linear fit to the data. The blue line shows the Moho depth that would be expected for Airy isostatically compensated topography. C) Line 2 Vp/Vs ratio estimates from stacking with a red line showing linear least squares regression. Most of the Vp/Vs values are in the average range around 1.75. D) Line 3 isostatic model including elevation (note scales for elevation and Moho depth). The blue line shows a calculation for airy isostasy assuming the same average densities as in A. The fit to the data is not as good near the coast unless we include additional buoyant material from the subducting oceanic crust. The crust could be expected to be slightly thicker than normal oceanic crust due to the proximity of the Nazca Ridge which is expected to have a crustal thickness of 18 km (Hampel, 2002). The effect of this addition on the isostasy is noted by the green dashed line which is a better match to the data. E) Line 3 Moho depth with a red line showing a polynomial regression curve to the data points. The blue line shows isostatic compensation depth and the green dashed line shows the correction for subducting oceanic crust. F) Line 3 Vp/Vs ratio showing a linear regression curve to the data. There appears to be a general trend from lower Vp/Vs values near the coast to higher values near Cusco.

Moho depths for Line 3 in figure 3.9 indicate isostatic compensation under much of the Altiplano but the fit to Airy isostasy is not as good near the coast where the slab depth is shallower, possibly as a consequence of the presence of the Nazca Ridge. The crust appears compensated within the uncertainty of the data if buoyant material is present near the coast with dimensions comparable to that of the Nazca Ridge (see figure 3.9D). The Vp/Vs ratio varies with most values falling between 1.7 and 1.8 with an average value of 1.75 and shows no strong trends other than an overall slight increase in Vp/Vs with distance from the coast.

3.4. Discussion

3.4.1 Moho Depth and Vp/Vs

The maximum Moho depth of 75 km beneath the Altiplano is consistent with results for the first seismic array (Line 1) in the region of normal subduction dip (Phillips et al,

2012).   Previous studies in the Central Andes have resulted in comparable estimates for

crustal thickness. Most estimates have an average value of 70 km with ranges between

59 and 80 km for crustal thickness beneath the Western and Eastern Cordilleras and

Altiplano (Baumont et al, 2001; Beck et al, 1996; Beck & Zandt, 2002; Cunningham &

Roecker, 1986; Lloyd et al, 2010; McGlashan et al, 2008; Myers et al, 1998; Yuan et al,

2002; Zandt et al, 1994). The crust in the Altiplano region is isostatically compensated

primarily through crustal thickening (Whitman et al, 1993), and crustal shortening due

to compression generated by plate coupling or through the Arica bend provides a

significant mechanism for contributing the crustal thickness. Gotberg et al (2010) show

that 70 km of thickness in to the Andes would require 240–300 km of shortening, but

their preferred shortening estimate left a significant proportion of this shortening budget

unaccounted for. Other possible mechanisms for thickening include processes such as

shortening related to the Arica bend (Kley & Monaldi, 1998; Gotberg et al, 2010),

magmatic additions or shortening hidden by the volcanic arc (Gotberg et al, 2010),

thermal weakening, upper mantle hydration (Allmendinger et al, 1997), or other factors.

Another possible mechanism which would help explain crustal thickness not accounted

for by shortening is tectonic underthrusting which would be consistent with the idea

that the midcrustal structure observed at 40 km depth is a result of underthrusting of the

Brazilian shield (Whitman et al, 1993). This mechanism is more consistent with a

gradual uplift model for this part of the Altiplano (Barnes and Ehlers, 2009; Ehlers and

Poulsen, 2009; McQuarrie et al., 2005; Elger et al., 2005; Oncken et al., 2006).

Vp/Vs ratios appear to have an average value between 1.73 and 1.75 with few

discernible patterns in terms of areas of higher or lower Vp/Vs. A Vp/Vs ratio of 1.73-

1.75 corresponds to a Poisson's ratio of 0.25 to 0.2576, which is compatible with previous results for the Altiplano (Beck et al, 1996; Swenson et al, 2000; Zandt & Ammon, 1995). The observed values of the Vp/Vs ratio support the conclusion that the crust in the transition and flat slab region are nonvolcanic since there are no regions with abnormally high values as might be expected where a magma body is present. The location of the active volcanic arc relative to the arrays can be seen in figure 3.1 which confirms that Lines 2 and 3 are located outside of the volcanic region. Vp/Vs results for Line 1 in the region of normal subduction showed a few areas of higher Vp/Vs values near the active volcanic arc, which may be indicative of magmatism (Phillips et al, 2012). The amount of variation in Vp/Vs measurements is partly due to uncertainty in cases where the multiples on which they rely are not readily apparent in the receiver function data resulting in less constraint on Vp/Vs results. An example is seen in the supplementary materials where the signal from the Moho is observed more clearly than the multiple arrivals. The uncertainty is given by the 95% contour line and gives a 1σ value of about 0.035 which is an average uncertainty estimate for error due to sources such as noise and unclear multiple arrivals.

3.4.2 Slab Structure

 The shape of the slab is deliniated through various images from different backazimuths and the use of both P/PP and PKP receiver functions. For Line 2 the slab signal appears as a primarily negative impedance signal (see figures 3.3, 3.5 and 3.7), which agrees with the finite-difference modeling results. The transition from normal (~30 degree) subduction near Juliaca to flat slab subduction near Cusco appears to be

gradual, thus there is no evidence that the subducting Nazca Ridge caused a break in the slab. A subduction transition, which appears as a smooth bend in the slab is consistent with seismicity results of Grange et al, 1984. If the slab were tearing we would expect to see a whole series of tears as the Nazca Ridge propagated down the coast. Note that the point where the slab is starting to flatten is some 400 km ahead to the projection of the Nazca ridge. There is no indication in the seismicity that the slab returns to normal dip after the passage of the Nazca ridge. Note the contrast with Central Chile where the uplift is 130 km ahead of the projection of the Juan Fernandez Ridge and returns to its original dip within 150 km in its wake (estimated from slab contours, see Anderson et al 2007).
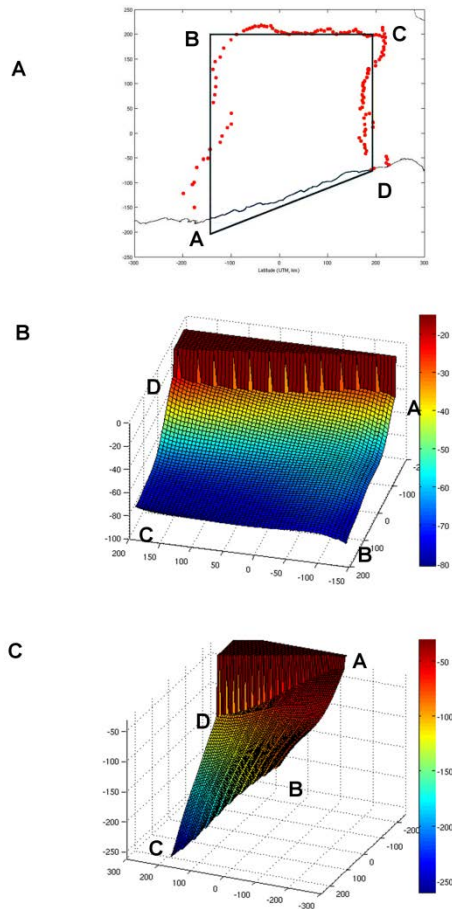
Figure 3.10. Interpolation of the Moho and slab estimates across the region enclosed by the seismic arrays in three dimensions. (A) Black lines represent region that was interpolated over. The letters correspond to corners of the 3D models below, (B) 3D model of the Moho depth, (C) 3D model of the slab.

The slab shape can be seen in a 3D model showing an interpolation of expected slab

and Moho depths for all of the arrays in figure 3.10. In contrast to the negative

impedance slab signal from the transition region, a positive impedance signal can be

seen for the flat slab region in figures 3.6-3.8. The strongest amplitude of the double

pulse slab structure can be seen in the first ~250 km of distance from the trench as the

slab is descending to a depth of 100 km. This may be a result of the deeper subduction

of hydrated oceanic sediments prior to dehydration of the minerals in the crust at

greater distances and depths (Kawakatsu and Watada 2007; Katayama et al. 2006). A

comparison of the models for the normal, transition, and flat slab regions and

corresponding synthetic receiver functions can be seen in figure 3.11 which has similar

velocities for all three 2D models. Thus the reason why the appearance of the slab

signal appears to be mainly a negative impedance signal for Line 2 compared to the

slab signals for the other two arrays appears to be related to the subduction zone

structure and angle of the subducted oceanic crust and a change in the transmission

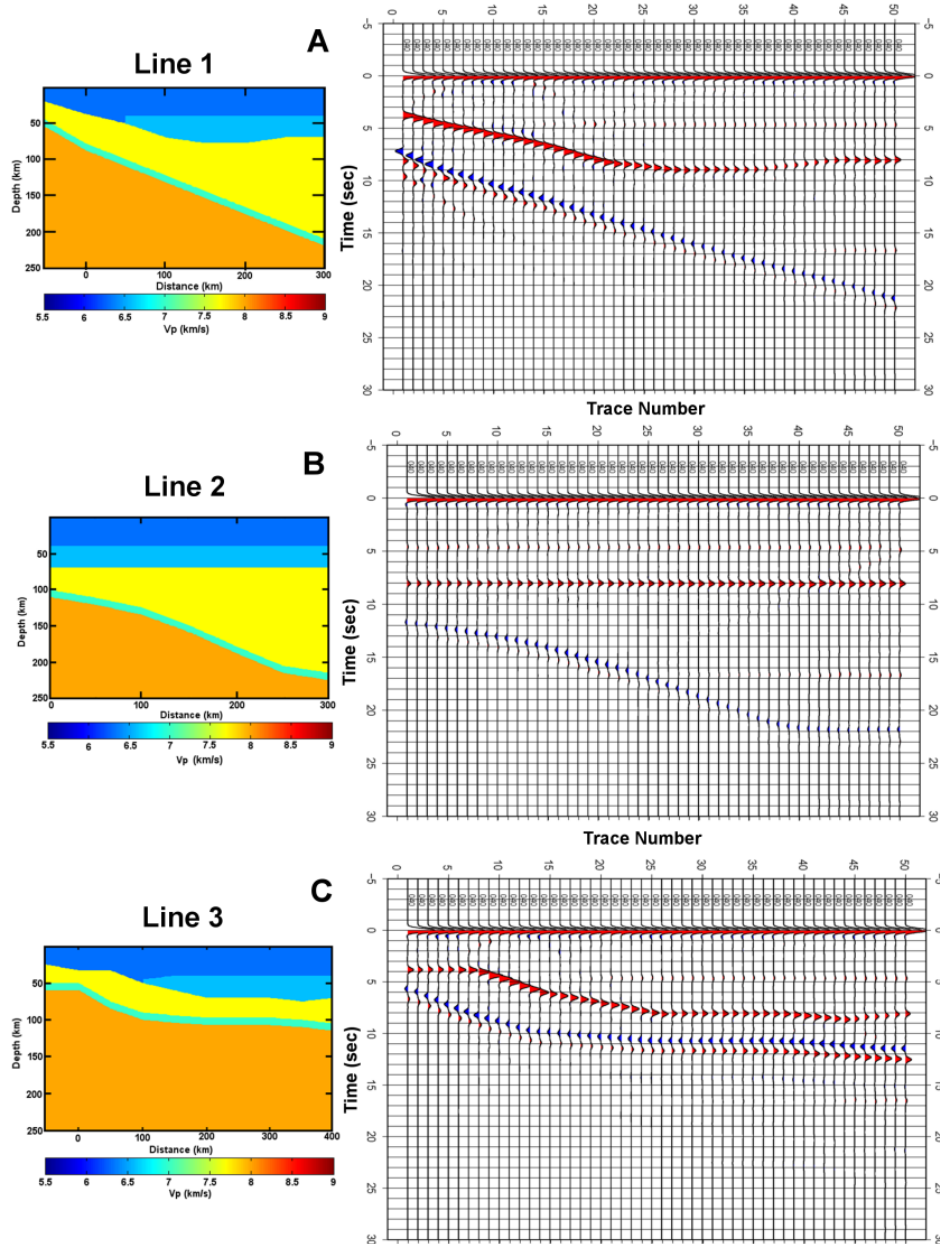coefficient for certain angles of incidence.

Figure 3.11. Comparison of synthetic models for all three seismic arrays showing A) the region of normal subduction (Line 1), B) the transition from normal to flat slab subduction (Line 2), and C) flat slab region (Line 3). Note that the synthetic receiver functions for Line 3 show a double pulse slab signal while the slab for Line 1 is double pulse mainly for the upper half and primarily negative at depth. The slab signal for Line 2 is mostly a negative impedance signal.

3.4.3 Nazca Ridge and Causes of Flat Slab Subduction

The Nazca Ridge is currently subducting at a latitude of -15˚ S and has a projection that puts the portion of the ridge that has already subducted just north of Line 3 (see figure 3.1). The Nazca Ridge has a trend of N42˚E at a region where the convergence direction is 77˚ resulting in an oblique angle of subduction and southward ridge migration (Hampel 2002). According to Hampel (2002), the Nazca Ridge began subducting at 11˚S at 11.2Ma and is presently migrating at 43mm/yr. Several authors have considered the buoyancy effect of the Nazca Ridge as a mechanism to support the development of flat slab subduction (Gutscher 1999; Gutscher, Spakman et al. 2000; van Hunen et al, 2002a, 2002b). The ridge is a wide feature (200km wide, 1.5km high, with a total crustal thickness of 17 km) so the stations on the array closest to the coast are most likely to show the impact of the subducting ridge on the subduction system. Some of the expected effects of the subducting ridge on the coastal region are deformation of the upper plate, uplift in the forearc, westward shift of the coastline (Hampel, 2002), and a gravity anomaly corresponding to the crustal root supporting the ridge (Hampel et al. 2004; Macharé & Ortlieb, 1992). The coastal stations show possible evidence of some uplift in the forearc compared to the normal subduction region but overall the elevation profiles are similar (see figure 3.13).
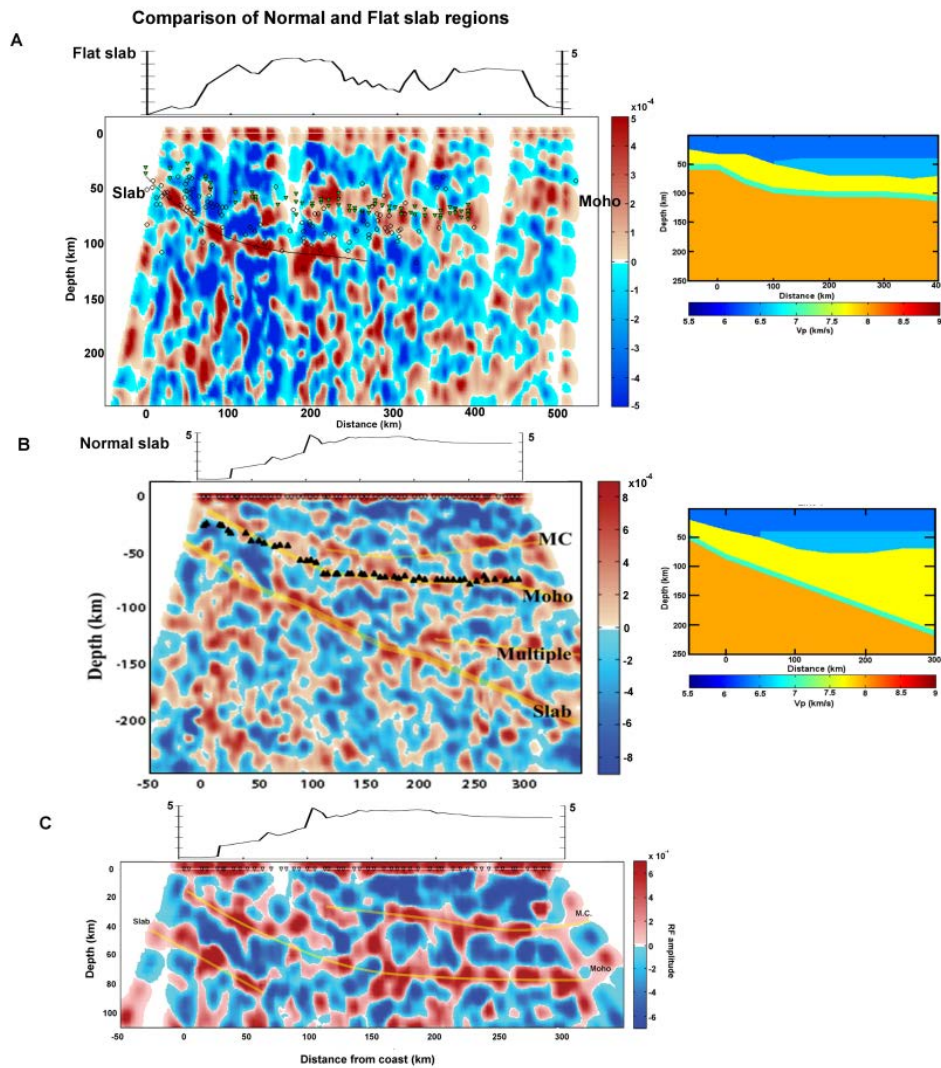
Figure 3.12. Comparison of the structure of the normal subduction region (Line 1) and flat slab region (Line 3). A) Line 3 from Nazca to Cusco. Moho picks from stacking are shown by green triangles. B) Results from Line 1 in the normal subduction region showing the 30 degree dipping slab using P/PP receiver functions from a NW backazimuth. Note that the double pulse slab signal from Line 3 (A) is most clear up to 100 km before appearing as a primarily negative signal while the slab in the region of normal signal is seen as a positive impedance signal at all depths down to a depth of about 200km. Simple models of the normal and flat slab regions used for finite difference modeling are shown to the right of the images. C) An image from Line 2 using P/PP receiver functions from all azimuthal directions showing only the upper 120 km. The Moho can be clearly seen as can a midcrustal structure at 40 km depth which is suggested to be from underthrusting of the Brazilian shield.

A comparison of receiver function results from Line 3 near the subducting Nazca Ridge with results from the region of normal subduction further south between Mollendo and Juliaca can be seen in figure 3.12. The slab dips near the trench are initially similar before the flat slab quickly flattens out at 100 km while in the normal region the slab continues descending at a constant angle. The Moho in both cases is relatively flat at a depth of around 70 km for much of the central section of the Altiplano. One notable difference is that the positive impedance signal from the Moho is less visible for Line 3 near the coastline where the slab is descending from the trench while for Line 1 the Moho is clear throughout the whole range of the array. The reason for this may be that dehydration could change the wedge velocity such that it has no contrast with the crust (Bostock et al. 2002). In the case of the flat slab, there is a gap of about 30 km between the Moho at 70 km depth and top of the slab at 100 km depth leaving a small amount of room for asthenospheric material. The difference between Moho depth and the subducting plate impacts the degree of coupling between the Nazca plate and overriding South American plate and thus the degree of intraplate hydrostatic suction which has been proposed as a possible factor in encouraging flat slab subduction.
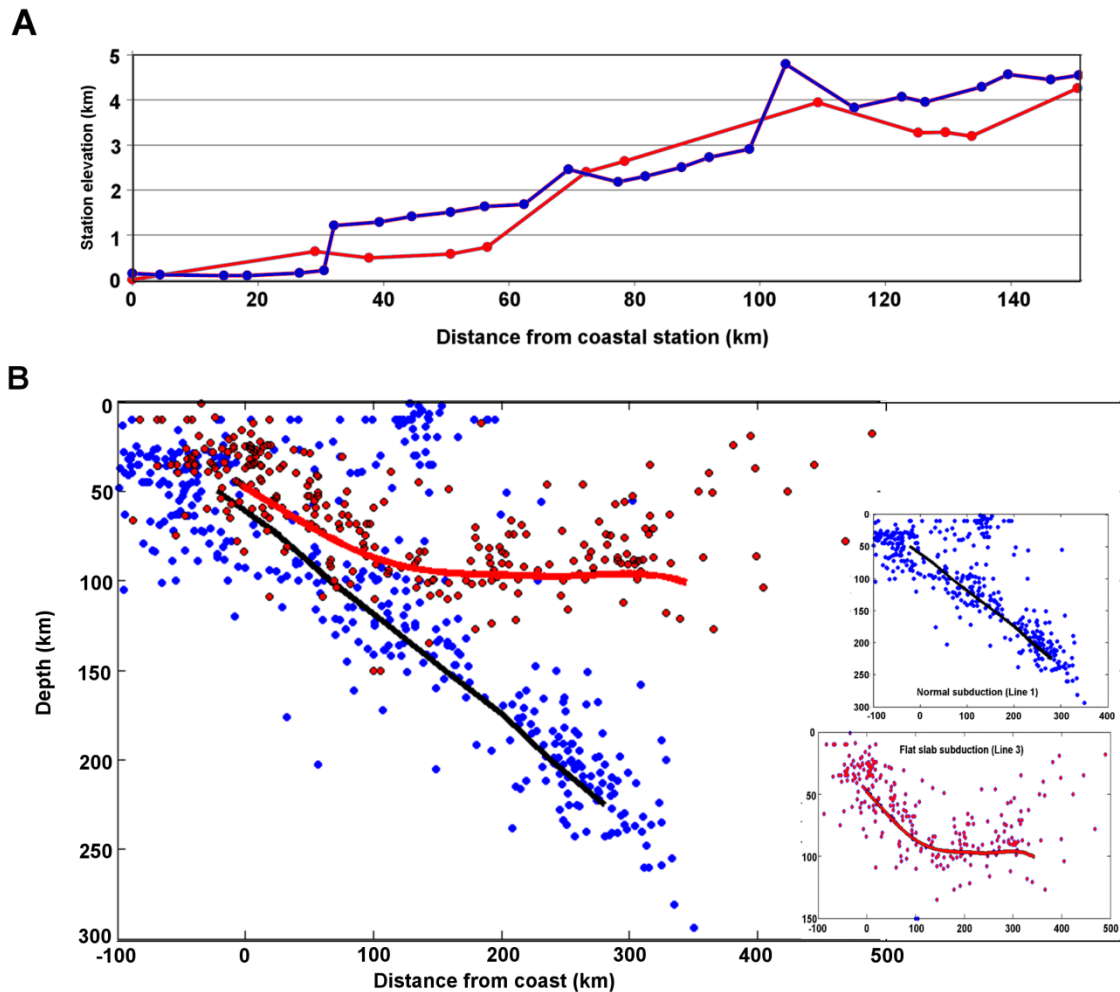
A

B

Figure 3.13. (A) Comparison of station elevation for Line 1 (normal subduction) and Line 3 (flat slab subduction). Line 1 elevation is shown by the blue line and Line 3 by the red line. (B) Depth versus distance seismicity cross section for Line 1 and Line 3 allowing for comparison of flat slab and normal subduction regions. The individual cross sections are shown as insets. Earthquakes are from the NEIC catalog from 1982 to 2012 for events of magnitude greater than 4.0. Solid lines show a fit to seismicity which gives the approximate location for the top of the subducting Nazca plate.

  A comparison of the topography in the forearc region to the Western Cordillera for

both the normal and flat slab region can be seen in figure 3.13A. Both exhibit a similar

rise although Line 1 is almost flat for the first 30 km before showing a sudden jump to

an elevation of about 1.2 km while Line 3 initially rises more rapidly before flattening

out until 60 km from the coast. Thus at a distance of 30 km from the coast, Line 3 has

an elevation about 400 m higher than Line 1 has at the same distance from the trench.

This may correspond to the several hundred meters of forearc uplift mentioned by

Hampel, (2002) as resulting from the subduction of the Nazca Ridge.

Figure 3.13B-D shows a comparison of the seismicity between the flat slab and normal

subduction region both in terms of seismicity in the Wadati-Benioff zone defining the

shape of the slab and crustal seismicity, which provides some measure of amount of

faulting and deformation in the upper plate. The seismicity comes from the NEIC

catalog for the past 30 years (1982–2012) including events larger than Mw 4.0. Events

were removed in which the depths were not well-defined and were given a default

crustal depth of 33 km. The overall number of events is greater in the south where

normal subduction is occurring. The difference in level of crustal seismicity does not

appear to be significant, although in the case of normal subduction there appears to be a

cluster of events near the center of the array at a very shallow depth, which is likely

related to activity near the active volcanic arc.

In terms of a cause of flat slab subduction, most authors conclude that the Nazca Ridge

does not have sufficient buoyancy by itself to sufficiently support the length of the

Peruvian flat slab (Gutscher, Olivet et al. 1999; Gurscher, Spakman et al. 2000; van

Hunen 2002a, 2004). Other factors present in Peru which can impact dip angle are the

fast subduction velocity relative to the motion of the overriding plate, intermediate age

of subducting lithosphere (30–40 Ma), the Arica bend, hydrostatic suction, and possibly

cycles of repeated slab breakoff and flat slab subduction since repeated flat subduction

events through time have been documented in the Andes (Haschke et al, 2007).

Although the main cause and relative importance of various causes are outside the scope of the data collected in this study, we conclude that the motion of the Nazca Ridge sweeping down the coast is unlikely to be a significant cause of flat slab subduction. The length of flat slab segment south of the Nazca Ridge appears too long to be supported by buoyancy of the Ridge alone and regions north of the Ridge do not return to normal dip after the Ridge has passed.

3.5. Conclusions

Receiver function studies from seismic arrays in Southern Peru provide more details of the structure of the transition region from normal (30 degree dip) subduction to flat slab subduction. The Moho beneath the Altiplano is found to have a maximum depth of 75 km. The shape of the slab is also clarified and the transition is found to be gradual from normal to flat slab subduction, which indicates that the change is most likely a contortion rather than a break in the slab. The slab is observed have an almost constant depth of 100 km beneath the array in the flat slab region. The observed impacts of the Nazca Ridge and flat slab subduction from this study are a lessening of overall seismicity, minor uplift in the forearc region, and a less defined Moho transition near the coast.

Chapter 3 References

· Abers, G. (2000), Hydrated subducted crust at 100-250 km depth, *Earth and Planet. Sci. Lett.*, 176, 323–330.

· Abers, G., P. van Keken, E. Kneller, A. Ferris, and J. Stachnik (2006), The thermal structure of subduction zones constrained by seismic imaging: Implications for slab dehydration and wedge flow, *Earth and Planet. Sci. Lett.*, 241, 387–397.

· Allmendinger, R., T. Jordan, S. Kay, and B. Isacks (1997), The Evolution of the Altiplano-Puna Plateau of the Central Andes, *Annu. Rev. Earth Planet. Sci.*, 25, 139–174.

· Ammon, C. (1991), The isolation of receiver effects from teleseismic P waveforms, *Bull. Seismo. Soc. Am.*, 81 (6), 2504–2510.

· Anderson, M., P. Alvarado, G. Zandt, and S. Beck (2007), Geometry and brittle deformation of the subducting Nazca Plate, Central Chile and Argentina, *Geophys. J. Int.*, 171, 419–434.

· Barazangi, M. and B. L. Isacks (1976), Spatial distribution of earthquakes and subduction of the Nazca plate beneath South America, *Geology*, 4, 686–692.

· Barnes, J. and T. Ehlers (2009), End member models for Andean Plateau uplift, *Earth-Sci. Rev*., 97, 105–132.

· Baumont, D., A. Paul, G. Zandt, S. L. Beck (2001), Inversion of Pn travel times for lateral variations of Moho geometry beneath the Central Andes and comparison with the receiver functions, *Geophys. Res. Lett*., 28 (9), 1663–1666.

· Beate, B., M. Monzier, R. Spikings, J. Cotton, J. Silva, E. Bourdon, and J. Eissen (2001), Mio-Pliocene adakite generation related to flat subduction in southern Ecuador: the Quimsacocha volcanic center, *Earth and Planet. Sci. Lett*., 192, 561–570.

· Beck, S. and G. Zandt (2002), The nature of orogenic crust in the central Andes, *J. Geophys. Res*., 107 (B10), 2230.

· Beck, S., G. Zandt, S. Myers, T. Wallace, P. Silver, and L. Drake (1996), Crustal-thickness variations in the central Andes, *Geology*, 24 (5), 407–410.

· Bevis, M. (1986), The Curvature of Wadati-Benioff Zones and the Torsional Rigidity of Subducting Plates, *Nature*, 323, 52–53.

· Bostock, M., R. Hyndman, S. Rondenay, and S. Peacock (2002), An inverted continental Moho and serpentinization of the forearc mantle, *Nature*, 417, 536–538.

· Cahill, T. and B. L. Isacks (1992), Seismicity and Shape of the Subducted Nazca Plate, *J. of Geophys. Res. - Solid Earth*, 97 (17), 503–17, 529.

· Cunningham, P. and S. Roecker (1986), Three-dimensional P and S Wave Velocity Structures of Southern Peru and Their Tectonic Implications, *J. of Geophys. Res*., 91 (B9), 9517–9532.

· Dorbath, C., M. Gerbault, G. Carlier and M. Guiraud (2008), Double seismic zone of

the Nazca plate in Northern Chile: High-resolution velocity structure, petrological implications, and thermomechanical modeling, *Geochem., Geophys., Geosys.*, 9 (7), Q07,006.

· Eakin, C. M., M. D. Long, S. L. Beck, and L. S. Wagner (2011), Seismic anisotropy and mantle flow beneath the Peruvian flat slab region, AGU, Fall Meeting 2011, abstract #DI44B-04.

· Ehlers, T. and C. Poulsen (2009), Influence of Andean uplift on climate and paleoaltimetry estimates, *Earth and Planet. Sci. Lett.*, 281, 238–248.

· Elger, K., O. Oncken, and J. Glodny (2005), Plateau-style accumulation of deformation: Southern Altiplano, *Tectonics*, 24, TC4020.

· Gotberg, N., N. McQuarrie, and V. Caillaux (2010), Comparison of crustal thickening budget and shortening estimates in southern Peru (12–14 S): Implications for mass balance and rotations in the "Bolivian orocline," *GSA Bulletin*, 122 (5–6), 727–742.

· Grange, F., J. Gagnepain, D. Hatzfeld, P. Molnar, L. Ocola, A. Rodrigues, S. Roeker, J. Stock, and G. Suarez (1984), The configuration of the seismic zone and the downgoing slab in Southern Peru, *Geophys. Res. Lett.*, 11 (1), 38–41.

· Gutscher, M., J. Malavielle, S. Lallemand, and J. Collot (1999), Tectonic segmentation of the North Andean margin: impact of the Carnegie Ridge collision, *Earth and Planet. Sci. Lett.*, 168, 255–270.

· Gutscher, M., R. Maury, J. Eissen, and E. Bourdon (2000), Can slab melting be caused by flat subduction? *Geology*, 28 (5), 535–538.

· Gutscher, M., J. Olivet, D. Aslanian, J. Eissen, and R. Maury (1999), The "lost Inca

Plateau": Cause of flat subduction beneath Peru?, *Earth and Planet. Sci. Lett.*,

171 (3), 335–341.

· Gutscher, M., W. Spakman, H. Bijwaard, and E. Engdahl (2000), Geodynamics of flat

subduction: Seismicity and tomographic constraints from the Andean margin,

Tectonics, 19 (5), 814–833.

· Hampel, A. (2002), The migration history of the Nazca Ridge along the Peruvian

active margin: a re-evaluation, *Earth and Planet. Sci. Lett*., 203, 665–679.

· Hampel, A., N. Kukowski, J. Bialas, C. Huebscher and R. Heinbockel (2004), Ridge

subduction at an erosive margin: The collision zone of the Nazca Ridge in southern

Peru, *J. of Geophys. Res.*, 109, B02101.

· Haschke M., A. Gunther, D. Melnick, H. Echtler, K. Reutter, E. Scheuber, and O.

Onken (2007), Chapter 16: Central and southern Andean tectonic evolution inferred

from arc magmatism, in *The Andes: Active Subduction Orogeny*, Frontiers Earth Sci.,

vol. 1, edited by O. Oncken et al., pp 337–354, New York: Springer.

· Haschke M., E. Scheuber, A. Gunther, and K. Reutter (2002), Evolutionary cycles

during the Andean orogeny: repeated slab breakoff and flat subduction?, *Terra Nova*,

14 (1), 49–55.

· Hayes, G. P., D. J. Wald, and R. L. Johnson (2012), Slab1.0: A three-dimensional

model of global subduction zone geometries, *J. Geophys. Res*., 117, B01302.

· International Seismological Centre, On-line Bulletin, http://www.isc.ac.uk, Internatl.

Seis. Cent., Thatcham, United Kingdom, 2010.

· Jischke, M. (1975), Dynamics of descending lithospheric plates and slip zones, *J.*

of Geophys. Res., 80, 4809–4813.

· Katayama, I., S. Nakashima, and H. Yurimoto (2006), Water content in natural

  eclogite and implications for water transport into the deep upper mantle, *Lithos*, 86,

  245–259.

· Kawakatsu, H. and S. Watada (2007), Seismic Evidence for Deep-Water

  Transportation in the Mantle, *Science*, 316, 1468.

· Kim, Y., R. W. Clayton, and J. M. Jackson (2010), Geometry and seismic properties

  of the subducting Cocos plate in central Mexico, *J. Geophys. Res.*, 115, B06310.

· Kley, J. and C. R. Monaldi (1998), Tectonic shortening and crustal thickness in the

  Central Andes: How good is the correlation? *Geology*, 26 (8), 723–726.

· Langston, C. (1979), Structure under Mount Rainier, Washington, inferred from

  teleseismic body waves, *J. Geophys. Res.*, 84, 4749–4762.

· Liggoria, J. and C. Ammon (1999), Iterative deconvolution and receiver function

  estimation, *Bull. Seism. Soc. Am.*, 89, 19–36.

· Lloyd S., S. van der Lee, G. Sand Franca, M. Assumpcao, and M. Feng (2010), Moho

  map of South America from receiver functions and surface waves, *J. of Geophys.

  Res.*, 115, B11315.

· Macharé, J. and L. Ortlieb (1992), Plio-Quaternary vertical motions and the

  subduction of the Nazca Ridge, central coast of Peru, *Tectonophysics*, 205, 97–108.

· McGeary S., A. Nur, and Z. Ben-Avraham (1985), Spatial gaps in arc volcanism: the

  effect of collision or subduction of oceanic plateaus, *Tectonophysics*, 119, 195–221.

· McGlashan N., L. Brown, and S. Kay (2008), Crustal thickness in the central Andes

  from teleseismically recorded depth phase precursors, *Geophys. J. Int.*, 175, 1013–

1022.

· McQuarrie, N., B. Horton, G. Zandt, S. Beck, and P. DeCelles (2005), Lithospheric

  evolution of the Andean fold-thrust belt, Bolivia, and the origin of the central

  Andean plateau, *Tectonophysics*, 399, 15–37.

· Myers, S., S. Beck, G. Zandt, and T. Wallace (1998), Lithospheric-scale structure

  across the Bolivian Andes from tomographic images of velocity and attenuation for

  P and S waves, *J. of Geophys. Res.*, 103 (21),233–21,252.

· Olbertz, D., M. Wortel, and U. Hansen (1997), Trench migration and subduction zone

  geometry, *Geophys. Res. Lett.*, 24, 221–224.

· Oncken, O., J. Kley, K. Elger, P. Victor, and K. Schemmann (2006), Deformation of

  the Central Andean Upper Plate System-Facts, Fiction, and Constraints for Plateau

  Models, Springer, Berlin, 569 pp.

· Pennington, W. (1984), The Effect of Oceanic Crustal Structure on Phase-Changes

  and Subduction, *Tectonophysics,* 102, 377–398.

· Phillips, K. E., R. Clayton, P. M. Davis, H. Tavera, R. Guy, S. Skinner, I. Stubailo, L.

  Audin, and V. Aguilar (2012), Structure of the Subduction System in Southern Peru

  From Seismic Array Data, *J. Geophys. Res.*, doi:10.1029/2012JB009540, in press.

· Pilger, R. (1981), Plate reconstructions, aseismic ridges, and low-angle subduction

  beneath the Andes, *GSA Bull.*, Part I, 92, 448–456.

· Ryan, J., K. Ward, R. Porter, S. Beck, G. Zandt, L. Wagner, E. Minaya, and H. Tavera

  (2011), Preliminary Results From the CAUGHT Experiment: Investigation of the

  North Central Andes Subsurface Using Receiver Functions and Ambient Noise

  Tomography, AGU, Fall Meeting 2011, abstract #T11B-2323.

· Sacks, I., 1983. The subduction of young lithosphere, *J. of Geophys. Res.*, 88, 3355–3366.

· Skinner, S. M. and R. W. Clayton (2012), The lack of correlation between flat slabs and bathymetric impactors in South America, *Earth and Planet. Sci. Lett.*, In Review.

· Suarez G., P. Molnar, B. C. Burchfiel (1983), Seismicity, Fault Plane Solutions, Depth of Faulting, and Active Tectonics of the Andes of Peru, Ecuador, and Southern Colombia, *J. of Geophys. Res.*, 88 (B12), 10403–10428.

· Swenson, J., S. L. Beck, and G. Zandt (2000), Crustal structure of the Altiplano from broadband regional waveform modeling: Implications for the composition of thick continental crust, *J. of Geophys. Res.*, 105 (B1), 607–621.

· van Hunen, J., A. van den Berg, and N. Vlaar (2002a), The impact of the South American plate motion and the Nazca Ridge subduction on the flat subduction below South Peru, *Geophys. Res. Lett.*, 29 (14).

· van Hunen, J., A. van den Berg, and N. Vlaar (2002b), On the role of subducting oceanic plateaus in the development of shallow flat subduction, *Tectonophysics*, 352, 317–333.

· van Hunen, J., A. van den Berg, and N. Vlaar (2004), Various mechanisms to induce present-day shallow flat subduction and implications for the younger Earth: a numerical parameter study, *Phys. of the Earth and Planet. Int.*, 146, 179–194.

· von Huene, R., J. Corvalan, E. R. Flueh, K. Hinz, J. Korstgard, C. R. Ranero, W. Weinrebe, and the Condor Scientists (1997), Tectonic control of the subducting Juan Fernandez Ridge on the Andean margin near Valparaiso, Chile, *Tectonics*, 16,

474–488.

· Whitman, D., B. L. Isacks, and S. M. Kay (1993), Lithospheric Structure and Along-Strike Segmentation of the Central Andean Plateau, 17-29˚ S, Second ISAG, Oxford (UK), 21-23/9/1993.

· Yan, Z. and R.W. Clayton (2007), Regional mapping of the crustal structure in southern California from receiver functions, *J. of Geophys. Res*., 112, B05311.

· Yogodzinski, G. M., J. M. Lees, T. G. Churikova, F. Dorendorf, G. Woerner, and O. N. Volynets (2001), Geochemical evidence for the melting of subducting oceanic lithosphere at plate edges, *Nature,* 409, 500–504.

· Yuan, X., S. V. Sobolev, and R. Kind (2002), Moho topography in the central Andes and its geodynamic implications, *Earth and Planet. Sci. Lett*., 199, 389–402.

· Zandt, G. and C. Ammon (1995), Continental crust composition constrained by measurements of crustal Poisson's ratio, *Nature*, v. 374, p.152–154.

· Zandt, G., A. Velasco, and S. Beck (1994), Composition and thickness of the southern Altiplano crust, Bolivia, *Geology*, 22, 1003–1006.

· Zhu, L. and H. Kanamori (2000), Moho depth variation in southern California from teleseismic receiver functions, *J. Geophys. Res*., 105 (B2), 2969–2980.